Naval Research Laboratory

Washington, DC 20375-5320

SHIMCAD Breadboard:
Design and Characterization

Christoph R. Englert

Upper Atmospheric Physics Branch
Space Science Division

David D. Babcock

Artep Inc.
Ellicott City, Maryland

John M. Harlander

St. Cloud State University
St. Cloud, Minnesota

October 16, 2006

REPORT DOCUMENTATION PAGE

1. REPORT DATE (DD-MM-YYYY)	2. REPORT TYPE	3. DATES COVERED (From - To)
16-10-2006	Memorandum Report	October 2005 - August 2006

4. TITLE AND SUBTITLE

SHIMCAD Breadboard: Design and Characterization

5a. CONTRACT NUMBER

5b. GRANT NUMBER

5c. PROGRAM ELEMENT NUMBER

6. AUTHOR(S)

Christoph R. Englert, David D. Babcock,* and John M. Harlander†

5d. PROJECT NUMBER

5e. TASK NUMBER

5f. WORK UNIT NUMBER
6564

7. PERFORMING ORGANIZATION NAME(S) AND ADDRESS(ES)

Naval Research Laboratory
4555 Overlook Avenue, SW
Washington, DC 20375-5320

8. PERFORMING ORGANIZATION REPORT NUMBER

NRL/MR/7640--06-8998

9. SPONSORING / MONITORING AGENCY NAME(S) AND ADDRESS(ES)

10. SPONSOR / MONITOR'S ACRONYM(S)

11. SPONSOR / MONITOR'S REPORT NUMBER(S)

12. DISTRIBUTION / AVAILABILITY STATEMENT

Approved for public release; distribution is unlimited.

13. SUPPLEMENTARY NOTES

*Artep Inc., Ellicott City, MD
†St. Cloud State University, St. Cloud, MN

14. ABSTRACT

This report covers the first phase of the Spatial Heterodyne Imager for Chemicals and Atmospheric Detection (SHIMCAD) project. The two goals of this phase were (1) to design and build a non-field-widened LWIR SHS breadboard interferometer with primarily off-the-shelf parts and using fixed angles and distances within the interferometer so that no post integration alignment is required and (2) to characterize the interferometer's wavelength calibration, phase distortion, and zero path location in order to verify that the approach of fixed optics locations and no alignment possibilities is adequate. The detailed results of this breadboard phase are presented here, showing the successful achievement of the above goals.

15. SUBJECT TERMS

Spatial heterodyne spectroscopy
Long wave infrared

16. SECURITY CLASSIFICATION OF:			17. LIMITATION OF ABSTRACT	18. NUMBER OF PAGES	19a. NAME OF RESPONSIBLE PERSON
a. REPORT	**b. ABSTRACT**	**c. THIS PAGE**	UL	35	Christoph R. Englert
Unclassified	Unclassified	Unclassified			**19b. TELEPHONE NUMBER** (include area code) (202) 767-5528

Contents

iii

SHIMCAD Breadboard
Spatial Heterodyne Imager for Chemicals and
Atmospheric Detection
Design and Characterization

1   Introduction

1.1   The SHIMCAD Project

The overall goal of the NRL Spatial Heterodyne IMager for Chemicals and Atmospheric Detection (SHIMCAD) project is to develop an intrinsically rugged, new type of long wave infrared (LWIR) hyperspectral sensor for the passive measurement of atmospheric trace constituents. SHIMCAD is a joint effort of the NRL Space Science Division, the NRL Remote Sensing Division and St. Cloud State University.

The project consists of three phases. A breadboard phase, a brassboard phase and a testing phase. The main objectives of those phases are:

- Breadboard Phase

    - Design and build a non-field-widened LWIR Spatial Heterodyne Spectroscopy (SHS) breadboard interferometer (1) with primarily off-the-shelf parts and (2) using fixed angles and distances within the interferometer so that no post integration alignment is required.

    - Characterize the interferometer's wavelength calibration, phase distortion, and zero path location in order to verify that the approach of fixed optics locations and no aligment possibilities is adequate.

- Brassboard Phase

    - Design and build a field-widened LWIR SHS brassboard interferometer with its étendue optimized for the étendue of the cooled array detector.

– Use the brassboard interferometer to build a compact brassboard spectrometer including a telescope, exit optics, array detector, and data acquisition

– Characterize the performance of the brassboard spectrometer in the laboratory

• Testing Phase

– Perform first ground based field measurements

– Perform a vibration test

– Perform test measurments using the NRL IR calibration facility

– If possible, perform observations from an airborne platform

This report covers the results of the successfully completed first phase of the SHIMCAD project.

1.2 Background

Passive IR spectroscopy has long been recognized and continues to be a valuable tool for detecting and identifying trace gases in the atmosphere. Examples of specific applications include the detection of toxic industrial chemicals, locating leaks of organic compounds, monitoring exhaust gasses at industrial facilities, or detecting chemical warfare agents.

The wavelength region between about 8-12 μm, is of particular importance for remote sensing (or standoff detection) because of several reasons: First, it is the so called finger print region in the LWIR, since it contains *unique* absorption/emission features of many molecules of interest. These spectral features are typically due to bending modes of the molecules. The second important reason is that the atmosphere is optically thin enough to allow standoff distances of several kilometers. The third advantage of this wavelength region is that measurements can be performed during day or night since the influence of sunlight on a typical thermal scene around 10 μm is generally small.

Many different types of instruments with a variety of spectral resolution, spatial resolution, bandpass, and radiometric performance have been developed in the

past for LWIR hyperspectral imaging of trace gasses from the ground and airborne platforms. Some examples are:

- SEBASS (Spatially Enhanced Broadband Array Spectrograph System) : A 1D imaging prism spectrograph that can be used from an airborne platform [Hackwell et al., 1996].

- AHI (Airborne Hyperspectral Imager): A grating spectrometer with 1D imaging capability [Lucey et al., 1998].

- AIRIS (Adaptive Infrared Imaging Spectroradiometer): An 2D imager with a tunable filter (Fabry Perot Interferometer) [Marinelli et al., 1999].

- JSLSCAD (Joint Services Lightweight Standoff Chemical Agent Detector): A non-imaging conventional Fourier Transform Spectrometer (FTS) which scans the field of view in two dimensions to achieve spatial coverage [Hammond and Popa, 2005]

- HiSPEC (Ultra-high sensitivity spectrometer): A non-imaging LWIR Fourier Transform Spectrometer [Schildkraut et al., 2002, 2004]

- Turbo FT: A non-imaging FTS in which the optical path is modulated by a rotating refractor [Wadsworth and Dybwad, 2002]

- FIRST (Field-portable Imaging Radiometric Spectrometer Technology): A 2D imaging FTS for which the two dimensional scene is imaged on the array detector and temporally modulated by a moving mirror [Vallières et al., 2005]

The above instruments can be grouped into three categories. First, diffractive spectrometers that use a grating or prism to observe the IR spectrum (SEBASS, AHI). These instruments record the entire spectrum in one exposure so that the measured spectrum is impervious to scene changes during the exposure. This "one shot" approach combined with the fact that they can be built without moving parts makes them particularly useful for applications from a moving platform like an airplane, UAV (Unmanned Aerial Vehicle), car, or truck. Diffractive spectrometers are able to image a maximum of one spatial dimension for each exposure using a two

dimensional detector array. To build up a hyperspectral cube with two spatial and one spectral dimension, the field of view of these instruments has to be scanned or used in a pushbroom geometry. Since diffractive spectrometers require a slit in the foreoptics, which especially for high resolving power, limits the accepted solid angle, a large aperture may be required to obtain adequate signal on faint emissions. This results in a larger, heavier instrument.

The second category is filter radiometers (like AIRIS). They use a tunable Fabry Perot filter to create 2D images at different, narrow band wavelength intervals. This instrument type acquires the spectral information in the time domain and cycles through the different filter transmittances quickly to minimize changing scene effects.

Fourier transform spectrometers are the third category (JSLSCAD, HiSPEC, Turbo FT, FIRST). They record the Fourier transform of the spectrum in the time domain by varying the optical path difference (OPD) in one or both arms of a Michelson interferometer. FTSs can image up to two spatial dimensions on a two dimensional detector array, but since the spectral information is gathered in the time domain, the scene must stay constant during the OPD scan. For practical field spectrometers, this means that the scan speed has to be high. All conventional FTSs have at least one moving part and require adequate metrology that determines the OPD for all samples of the interferogram scan.

At this point, one might ask the question: "Which instrument type is best for LWIR remote sensing?" This question has been addressed in the literature e.g. by Pritt et al. [1997] or Sellar and Boreman [2005]. The most important common conclusion is that the best choice of technique depends on the individual set of requirements and constraints of the application including the spectral resolution, spectral range, spatial resolution, spatial scan speed, platform stability, variability of the scene, available detector size, and the performance of the available detectors.

The primary objective of the SHIMCAD project is the development of an innovative type of LWIR spectrometer that does not fit in any of the above categories, but combines some of their advantages. Like a dispersive spectrometer, it is a one shot technique that does not require moving parts, yet it also has the high interferometric throughput with the additional option of field-widening using fixed optics. It can image one spatial dimension in one exposure and can be built in a compact,

rugged package. These features of SHS make it a primary candidate for LWIR field spectroscopy, specifically for applications that use a moving or jittering platform and require moderate spatial resolution at high sensitivity.

The potential advantages of SHS for the LWIR have been recognized before and led to an effort to build such an instrument at the Los Alamos National Laboratory (LANL) [Laubscher et al., 1999 and references therein]. The LANL work produced a first monochromatic LWIR SHS interferogram but was not continued for programmatic reasons. In this work we do not follow the exact LANL approach, but build on SHS experience which we have gathered in the ultraviolet and visible/near IR [Harlander et al., 1992; 1994; 2002; 2003; Cardon et al., 2003; Englert et al., 2004; 2006; 2006]. A comparison between the first LANL laboratory result and our first results is included in this report.

In the past, NRLs Space Science Division in cooperation with St.Cloud State University has built a proof-of-concept UV SHS instrument for middle atmospheric remote sensing named SHIMMER (Spatial Heterodyne Imager for Mesospheric Radicals) which was flown on the Space Shuttle in 2002 [Harlander et al., 2002; Cardon et al., 2003]. An improved version of SHIMMER [Harlander et al., 2003] is scheduled to be launched in late 2006 as the primary payload of STPSat-1, a DoD Space Test Program mission. Recently, we also built a visible/near IR SHS breadboard instrument to explore hyperspectral fire detection [Englert et al., 2005].

In section 1.3 the SHS concept is described, providing a basis for the following detailed description. In section 1.4 the imaging approach that we plan to use in the following phases of the SHIMCAD project is outlined. This approach is fundamentally different from the one proposed previously by LANL. In sections 2 and 3 the SHIMCAD breadboard design and the results of its characterisation are presented.

1.3   Basic Concept of Spatial Heterodyne Spectroscopy

Spatial Heterodyne Spectroscopy is a relatively novel optical technique. It was developed in the late 1980s at the University of Wisconsin for ultraviolet remote sensing [Harlander, 1991]. To date, SHS has mainly been applied in the ultraviolet spectral region, where SHS allows the design of very high spectral resolution and high throughput instruments that are particularly small and rugged.

The basic concept of SHS is described in detail in publications by Harlander et al. [1992, 1994, 2003]. The concept is similar to a Michelson interferometer with the return mirrors replaced by fixed, tilted diffraction gratings. Figure 1 shows the basic SHS concept.

For each exposure, the detector array in an SHS spectrometer records an entire interferogram. The ideal SHS interferogram can be written as [Harlander, 1991]:

$$I(x) = \frac{1}{2} \int_0^\infty B_\sigma(\sigma) \left[1 + \cos\left\{ 2\pi[4(\sigma - \sigma_0) \tan\theta_L]x \right\} \right] d\sigma \qquad (1)$$

where $B_\sigma(\sigma)$ is the wavenumber dependent spectral density, σ_0 is the Littrow wavenumber for which the recorded fringe frequency is zero, θ_L is the grating angle, and x is the pixel location. The leading factor of $1/2$ accounts for the fact that, as in FTS, half of the incident signal leaves the interferometer through the input port and, ideally, half is detected at the output port. Equation 1 shows that for a monochromatic source, an SHS instrument measures a cosine fringe pattern with a spatial frequency that is proportional to the difference of the incident wavenumber and the Littrow wavenumber. This "heterodyned" spatial frequency, together with the fact that the interferogram is measured in the spatial domain gives SHS its name. Using the definition of the heterodyned fringe frequency $\kappa \equiv 4(\sigma - \sigma_0) \tan\theta_L$ and the heterodyned spectral density $B(\kappa) \equiv [B_\sigma(\sigma_0 + \kappa/4\tan\theta_L) + B_\sigma(\sigma_0 - \kappa/4\tan\theta_L)]/4\tan\theta_L$ we can write:

$$I(x) = \frac{1}{2} \int_0^\infty B(\kappa) \left[1 + \cos\left\{ 2\pi\kappa x \right\} \right] d\kappa \qquad (2)$$

Equation 2 shows that the heterodyned spectral density can be recovered from the measured interferogram simply by subtracting the unmodulated offset and performing a Fourier transform on the remaining modulated part.

Some important properties of SHS are:

- SHS has no moving parts and can be built in a very rugged, compact package.

- SHS has high, interferometric throughput like Fourier transform spectrometers (FTS). In contrast to grating spectrographs, no slit is required in the fore optics. Thus, SHS instruments typically allow for higher throughput than
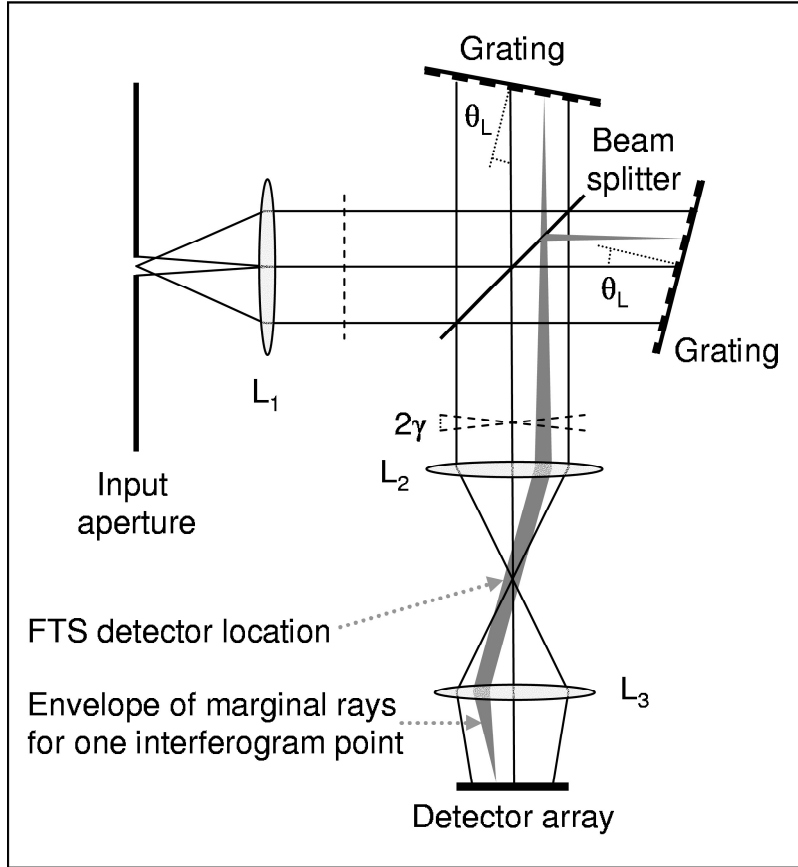
6

Figure 1: *Basic SHS concept. An incident wavefront (dashed line) is divided into the two interferometer arms by a beamsplitter. The two arms are terminated by fixed, angled diffraction gratings that tilt the wavefronts with respect to the optical axis. The tilt angle is proportional to the heterodyned wavenumber of the signal ($\gamma \propto [\sigma - \sigma_0]$), where σ_0 is the Littrow wavenumber of the gratings which is determined by the grating grove density and grating angle (θ_L). The tilted wavefronts are recombined at the beamsplitter and form Fizeau fringes at the detector array. In this example, the wavefronts are crossed in the middle, which yields a double sided interferogram with zero path difference in the middle and increasing path differences toward the edges of the array. The lenses L_i represent the telescope and exit optics. Note that, like in an FTS, the input optics does not require a slit. However, unlike a typical, single element FTS detector which collects the light in the indicated location, the SHS detector array is in the image plane of the gratings, which allows the detection of the interferogram without scanning.*

grating spectrographs, especially at high spectral resolution.

- SHS interferometers can be field-widened with a fixed prism in each interferometer arm (i.e. without moving parts).

- In contrast to conventional FTSs which record the interferogram in the time domain, SHS interferometers allow the simultaneous detection of all path differences with an imaging detector. This makes it a single shot technique, like a conventional grating spectrometer. This property is particularly important if the scene is rapidly changing during a measurement, which would otherwise contaminate the interferogram.

- In SHS, the maximum spectral bandwidth is limited by the combination of the number of detector array elements in one dimension and the resolving power.

- Like FTS, SHS is subject to multiplex noise, which compared to a grating spectrometer with equal throughput results in a signal to noise ratio (S/N) disadvantage for a photon shot noise limited detector. However, especially for high spectral resolution, SHS has a throughput advantage, that can be used to compensate or overcompensate this effect to achieve an equal or higher S/N. In case the measurement is detector noise limited instead of shot noise limited, the multiplex disadvantage turns into a multiplex advantage [Brault, 1985].

1.4 Imaging Approach

The one dimensional imaging approach that we will use for the SHIMCAD brassboard (Phases 2 & 3 of this project) is shown in Figure 2. The field of view (FOV) is imaged in one dimension on the focal plane array (FPA) while the other dimension on the FPA is used to record the interferogram (i.e. the spectral information). To ensure that the spatial variation within one spatial element of the FOV does not contaminate the interferogram, an anamorphic telescope will be used, similar to the SHIM-Fire breadboard [Englert et al., 2005]. Using SHS with this kind of input optics allows the single shot operation which preserves the insensitivity to a changing scene or pointing jitter. Note that this is fundamentally different from the LANL approach [Smith and Harlander, 1999] which does not allow single shot operation and thus is sensitive to a changing scene. Also note that for the breadboard
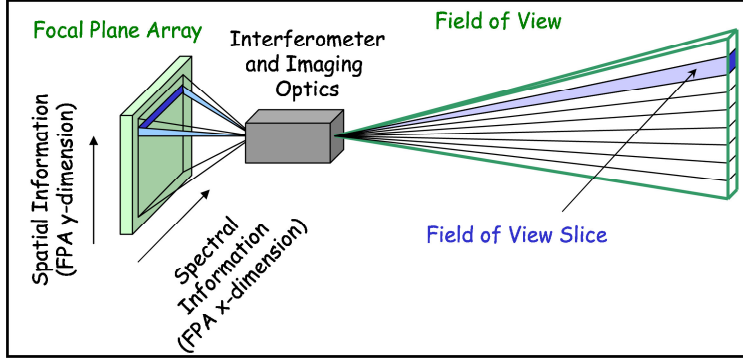
Figure 2: *Viewing geometry concept: The field of view (FOV) is composed of slices. The signal of each slice forms a complete interferogram in the x-dimension of the focal plane array. In order to guarantee that the spatial structure of the scene within a FOV slice does not contaminate the interferogram, an anamorphic telescope is used, which causes the scene to be out of focus in the x-dimension but in focus in the y-dimension of the FPA.*

development which we report on here, no anamorphic telescope was used, since the focus of this first project phase was to build and characterize a basic LWIR SHS interferometer.

2   SHIMCAD Breadboard Design

2.1   Interferometer Design Goals

Mechanical Design Goals:

For an LWIR SHS interferometer, we expect that the basic positioning tolerances of the optical components could be met by conventional CNC (computer numerically controlled) milling machines which typically achieve a precision of $\pm 0.5/1000$ inches ($\approx \pm 13\,\mu m$) and ± 30 arcseconds. Therefore, our goal was to design an interferometer structure that fixes all optical components without the requirement or option of any further position or angle adjustment. This has three advantages: (1) the interferometer does not require any time consuming alignment after it is assembled, (2) the structure can be built very compact and rugged, and (3) the fabrication of the structure is inexpensive.

9

Breadboard Optical Design Goals:

The overall optical design goal for this breadboard was to create a simple, non-field-widened interferometer with mainly commercial off-the-shelf (COTS) components and specifications close to the requirements of atmospheric remote sensing applications:

Spectral Resolution: The optimal spectral resulution for tropospheric standoff detection is driven by the shape of the emmission/absorption features. A spectral resulution of $4\,\text{cm}^{-1}$ is genernally regarded as optimal for passive LWIR trace gas detection and identification in the troposphere. It is therefore a common performance specification of other LWIR sensors such as JSLSCAD [Hammond and Popa, 2005] and FIRST, which is optimized for a $4\,\text{cm}^{-1}$ resolution [Vallières et al., 2004]. In the wavelength domain a $4\,\text{cm}^{-1}$ resolution at 1000cm^{-1} corresponds to a $0.04\mu m$ resolution at $10\mu m$. Our goal was to achieve a resolution of $4\,\text{cm}^{-1}$ or better after apodization of the interferogram. Apodization, e.g. with a Hanning function, provides a simple, localized instrumental line shape function in the spectrum, but decreases the resolving power by about a factor of two. Therefore, our goal was to achieve an unapodized resolution of $2\,\text{cm}^{-1}$ or better, which is equivalent to a resolving power of $\geqslant 500$ at $1000\,\text{cm}^{-1}$ or $10\,\mu m$.

Spectral Bandpass: To optimize the information for tropospheric trace gas detection and identification the bandpass should cover the entire $8\text{-}12\,\mu m$ atmospheric window or at least a major part of this window region. For the breadbord instrument, with which we did not plan to make any field measurement, this is not a primary requirement. Instead, a suitable COTS bandpass filter with transmittance in the $10\,\mu m$ window was selected.

Littrow wavenumber: The Littrow wavenumber is the wavenumber around which the spectrum is heterodyned and for which the spatial frequency in the interferogram is zero. The fringe frequency increases for increasing *and* decreasing wavenumbers (see equation 1). Our goal was to place the Littrow wavenumber at one edge of the spectral bandpass filter. This way the recovered spectrum is unique since only signal from one side of the Littrow wavenumber (single sideband) contributes to the interferogram. Specifically, we planned to place σ_0 at the low wavenumber cut-off of the filter rather than at the high wavenumber cut-off, because the fringe contrast and therefore sensitivity is slightly *higher* for low fringe frequencies (at low

wavenumbers) due to the point spread function on the detector and the finite pixel width. This way, we anticipate that the instrument sensitivity be more constant across the bandpass.

Phase distortion: Since the only other SHS LWIR interferometer, built by LANL [Laubscher et al., 1999], showed a large amount of phase distortion, one of our goals was to verify that the breadboard instrument does not produce fringes with equally severe phase distortion. To minimize the phase distortion, the flatness of the COTS interferometer components was an important criterion during their selection.

2.2   Interferometer Design and Integration

Overall interferometer geometry: We chose a hexagonal interferometer geometry in which the optical axis intersects the beamsplitter at a 30° angle [Harlander et al., 2003]. This reduces polarisation effects because the angle of incidence is farther from the Brewster angle ($\theta_B \approx 67°$ for ZnSe around $10\,\mu m$) than with the 45° geometry shown in Figure 1. Reduced polarization effects are directly linked to a higher beamsplitter efficiency and thus a instrument higher sensitivity.

Interferometer structure: The interferometer structure was designed to be a compact, rugged two-part block, which forms the hexagonal interferometer body. The beamsplitter is mounted between the two blocks and is registered against one surface of one of the blocks. The compensator plate is positioned next to the beamsplitter with a small airgap. The gratings are mounted on two sides of the interferometer body. Again, they are registered against surfaces of the interferometer blocks, which define their position and angle with respect to the optical axis and the beamsplitter. A schematic of the complete interferometer structure is shown in Figure 3. Detailed drawings of the two interferomter blocks are shown in Figures 4 and 5. Note that the interferometer structure is not a regular hexagon, since the gratings are tilted by the Littrow angle with respect to the optical axis. This Littrow angle is built into the interferometer blocks.

The interferometer structure was machined out of aluminium as two halves, with the beamsplitter and compensator plate mounted between the halves. After the compensated beamsplitter was installed the two halves of the interferometer were bolted together to form a rugged, compact entity. The last step in assembling
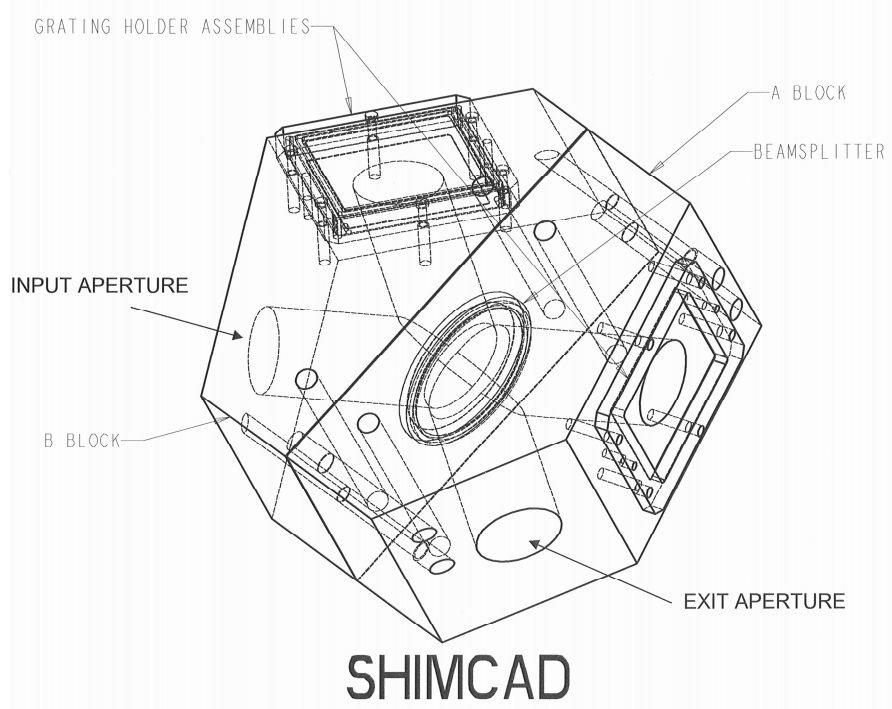
Figure 3: *Schematic of the SHIMCAD interferometer structure. The beamsplitter and compensator plate are sandwiched between the interferometer blocks. The beamsplitting surface is registered to a surface on block B. The grating holders attach the diffraction gratings directly to the face of hexagonal interferometer block ensuring the critical angle alignment when installing the gratings. The interferometer block was CNC machined out of aluminium.*

the interferometer was to install the gratings onto the two faces of the structure using the grating holders as shown in Figures 3 and 6.

Optical Design: All COTS components that were chosen for the SHIMCAD breadboard interferometer are listed in Table 1.

A compensator plate was placed parallel to the plate beamsplitter since the dispersion of ZnSe over the bandpass cannot be neglected. Over the bandpass of the filter, the change in refractive index[1] is about $8 \cdot 10^{-3}$ which, for an uncompensated, 3 mm thick plate beamsplitter, results in an optical path variation of about 2.5 λ. This wavelength dependent optical path leads to a wavelength dependent phase shift in the interferogram that can be corrected in post processing [Englert et al.,
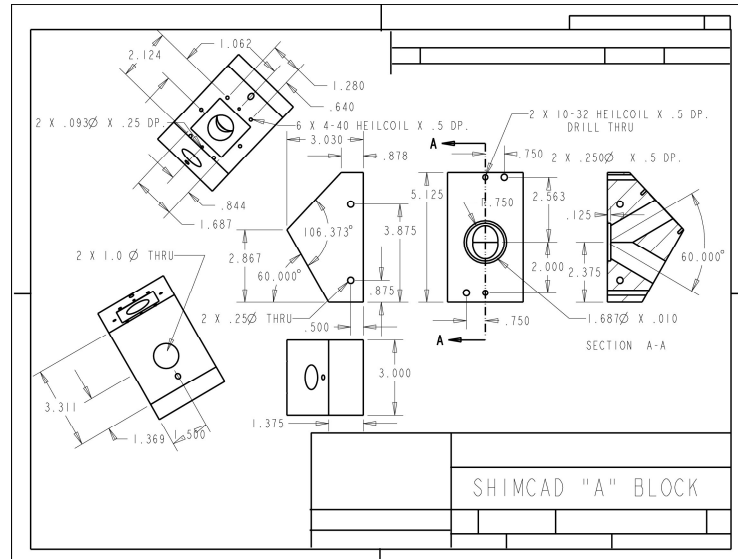
---

[1]http://www.luxpop.com/

Figure 4: *Drawing of SHIMCAD interferometer structure block A which shows the inset made to allow for the installation of a ZnSe compensator plate. It matches the thickness of the ZnSe beamsplitter, producing an optically compensated beamsplitter.*
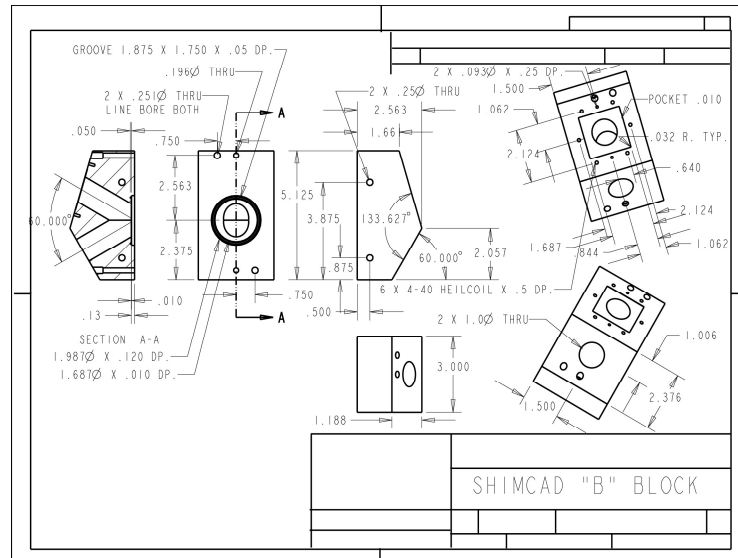

Figure 5: *Drawing of SHIMCAD interferometer structure block B. It shows the space allotted for the beamsplitter in the center, where the two beams from the diffraction gratings interfere.*

| Part	Properties	Part #
Beam-splitter	Maufaturer: Janos Substrate Material: ZnSe Thickness: 3 mm Flatness: $\lambda/2$ @ 633 nm Efficiency: 50% / 50%	A1225F638
Compensator plate	Manufacturer: Infrared Optical Products Substrate Material: ZnSe Thickness: 3 mm Coating: IR AR 8-12 μm	–
Bandpass filter	Manufacturer: Spectrogon Bandpass: 9.65-11.25 μm Average Transmittance: 76.7%	BBP-9650-11250c nm
Gratings	Manufacturer: Newport Corporation Groove density: 41.885 mm^{-1} Coating: Al Curvature: plano Blaze Wavelength: 10.6684 μm Blaze Angle: 12.80° Blank Material: BK Blank Size: 50×50×6 mm^3 Ruled Area: All	33010BK01-842R

Table 1: *Interferometer parts list*
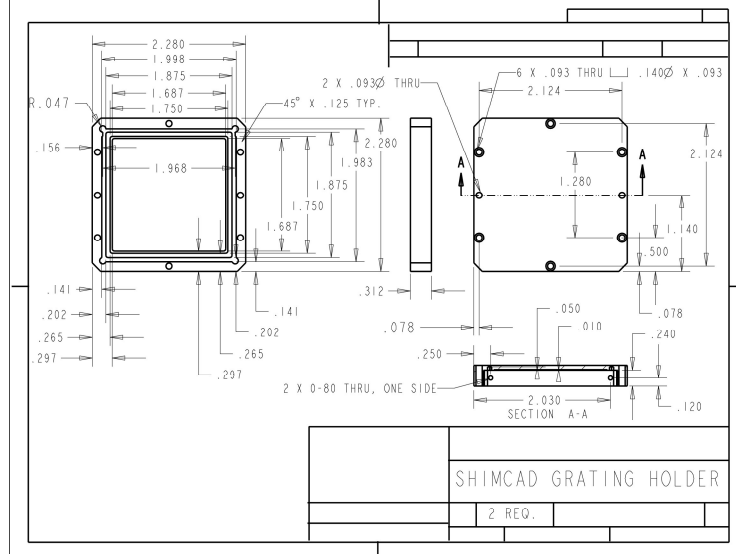
Figure 6: *Drawing of the SHIMCAD grating holders which are used to mount the gratings onto to the interferometer blocks. The position of the gratings is determined by the two surfaces of the interferometer body against which they rest.*

2004] but can result in decreased sensitivity to broadband signals. In addition, it makes it more difficult to find the zero path difference (ZPD) location of the interferogram, since the interferogram spike at zero path shows much less contrast when a broadband source is observed (see Section 3.3). The compensator plate minimizes the phase shift and maximizes the contrast of the zero path spike.

The bandpass filter was selected because it was a reasonable match to the banpass requirement and it is available off-the-shelf. The selection of the filter determined the design Littrow frequency to be λ_L=11.25 μm, at the long wave (short wavenumber) filter cut-off.

The gratings were chosen from COTS available products with the design goals as a guideline. Assuming an illuminated grating width[2] W of 1 cm, and the relationship

---

[2]At the time of the grating selection it was not known what detector would be available to do the SHIMCAD breadboard characterisation measurements. However, the detector on order for the second project phase has a width of $\approx$ 1 cm. With an exit optics magnification of unity, this would result in an effective grating width of $\approx$ 1 cm. The detector and effective grating width that were ultimately used in the breadboard characterization are discussed in Section 2.3

between W and the resolving power R:

$$R = \frac{2W}{d} \tag{3}$$

we found that the grating needed a groove density $(1/d)$ of $\geqslant 25\,\text{mm}^{-1}$ to achieve a resolving power or 500 or higher. After reviewing available COTS gratings, we selected gratings with a groove density of $41.885\,\text{mm}^{-1}$. The selection of the gratings determined the Littow angle θ_L (see also Figure 1):

$$\theta_L = \arcsin\frac{\lambda_L}{2d} = \arcsin\frac{1}{2d\sigma_0} = 13.63° \tag{4}$$

Using the above selections and assuming an illuminated grating width of $1\,\text{cm}$, we calculated the spatial fringe frequency at the gratings, f_x, as a function of wavenumber using the small angle approximation:

$$f_x \approx 4|(\sigma - \sigma_0)|\tan\theta_L \tag{5}$$

To cover the entire bandpass of the filter, the highest fringe frequency that needed to be detected is therefore:

$$f_x^{max} \approx 4(1036\,\text{cm}^{-1} - 889\,\text{cm}^{-1})\tan(13.63°) \approx 143\,\text{cm}^{-1} \tag{6}$$

This result meant that the detector array which was going to be used to record the interferogram had to have at least $2 \times 143 = 286$ pixel per centimeter in order not to encounter aliasing of the fringes. This is a reasonable pixel density specification for currently available detectors.

2.3 Spectrometer Set-Up

To set up the SHIMCAD breadboard spectrometer with the above interferometer, we also required an LWIR array detector, input optics, and exit optics that image the fringe localisation plane onto the detector. A picture of the set up is shown in Figure 7.
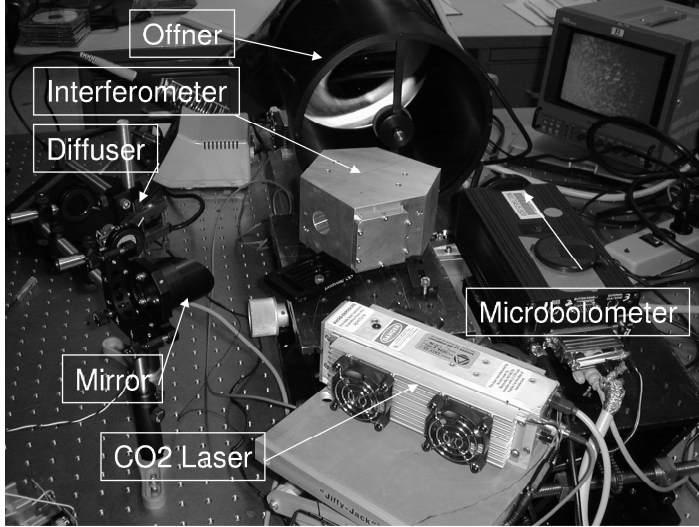
Figure 7: *This photograph shows the SHIMCAD breadboard setup with the laser source. The laser illuminates the diffuser, which feeds the parabolic mirror. The resulting signal is incident on the input aperture of the interferometer. The Offner relay images the grating plane (= fringe localisation plane) on to the microbolometer focal plane array.*

Input optics: For the input optics we selected a gold coated, off-axis parabolic mirror (Effective focal length: 76.2 mm from Janos Tech., Part # A8037-262). The mirror was illuminated from an iris positioned one focal length away from the mirror. With this geometry and a diffuse source at the iris, the angular extent of the beam incident on the interferometer was defined by the diameter of the iris.

Exit optics: The exit optics images the fringe localisation plane at the gratings onto the focal plane array. For this breadboard instrument we used an Offner relay, which resulted in a magnification of unity.

Detector / Focal plane array: For this breadboard effort, the MCT (Mercury Cadmium Telluride) detector that we plan to use for the second phase of the SHIM-CAD project was not yet available. Therfore, we used a Boeing microbolometer detector (Model SE-U20), with a 320×240 pixel focal plane array. The VO_x (vanadium oxide) detector array has a 51μm pixel pitch, and is sensitive between 8-14μm. The microbolometer has two outputs, an analogue output sent to a viewing monitor and a digital output connected to a personal computer. Digital images from the
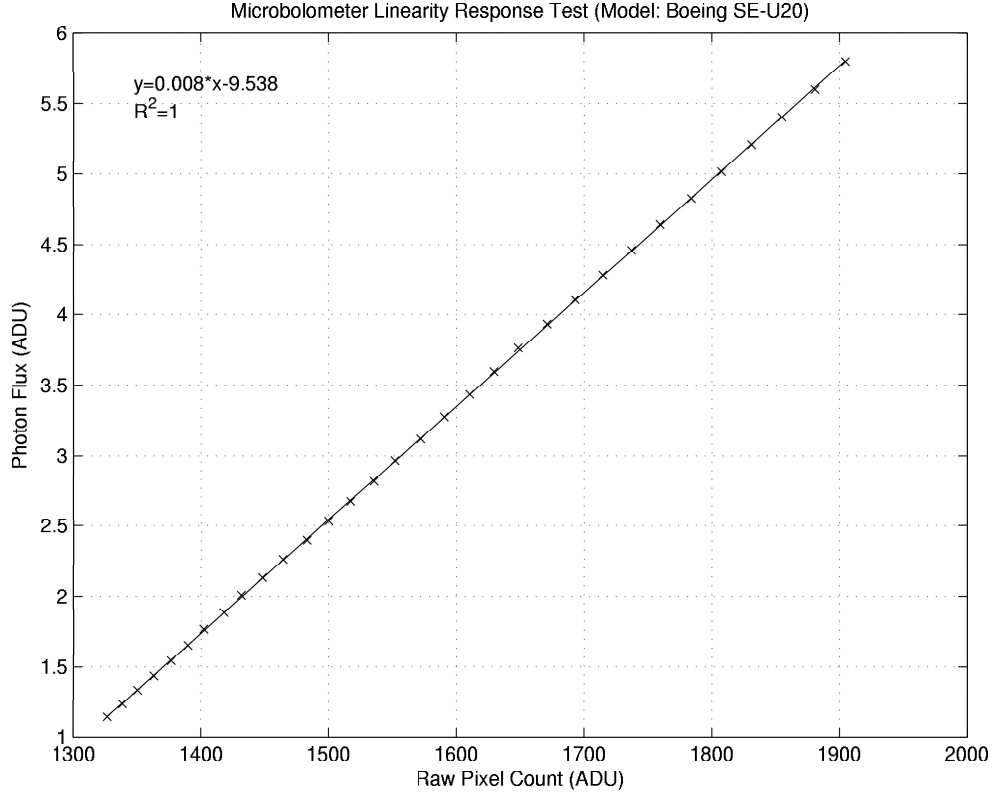
Figure 8: *The response linearity of the microbolometer array was verified by observing a calibrated blackbody at different temperatures using a constant integration time. This figure shows the change in response (counts after analog to digital conversion) versus the number of photons reaching the detector. The result shows adequate linearity for the entire brightness range that was accessible using the blackbody.*

microbolometer were saved as raw 16-bit numbers.

Similar to detectors in FTS instruments, the detector used in an SHS instrument has to have a linear response in order to avoid ghost features in the retrieved spectrum [Brault, 1985, Englert et al., 2005]. Therefore, before the microbolometer was used to image the output of the breadboard SHS interferometer, the linearity of the detector response was tested and verified for a limited signal range with a calibrated black body source at different temperatures. The result of the linearity test is shown in Figure 8.

Sources: For the characterization of the breadboard interferometer, a tunable

monochromatic source and a polychromatic source were used. The low output power CO_2 laser "Lasy-2S", manufactured by Access Laser Company, was used as the tunable spectral line source. It has a maximum output power of $100\,\text{mW}$ and can be tuned to different CO_2 lines by changing the laser's cavity temperature. To avoid laser speckles within the fringe image, we used a rotating sintered metal disk at the location of the input iris of the input optics, which creates a pseudo-diffuse, monochromatic source. As a polychromatic source, a simple coiled resistance wire filament (Boston Electronics IR-12K Series, 1250K at 6V) was used.

3 SHIMCAD Breadboard Characterization

3.1 First Fringe Pattern Observations

The first interferograms were observed using the CO_2 laser as a source. Figure 9 shows two raw interferograms in the two left panels. The interferograms correspond to two different laser cavity temperatures and consequently two different laser wavelengths. For each interferogram, one horizontal pixel row of the 2D array is displayed. Monochromatic fringe patters with high frequencies (76 and 127 fringes per detector width) can clearly be seen on a large unmodulated offset. This unmodulated offset is primarily caused by dark signal and thermal signal which does not originate from the laser. To eliminate this contribution, we took exposures with the laser off and subtracted them from the line measurements. The results of this "source-off" subtraction are shown in the right panels of Figure 9. The resulting fringe pattern has high contrast for almost the entire imaged grating width. The variation of the fringe pattern envelope is most likely caused by a combination of flat-field effects, including the illumination of the gratings. The higher fringe frequency shows lower contrast as expected from the imaging point spread function and the contribution from off axis signal. We have not performed any further optimization of the breadboard spectra like flatfielding, phase correction, or more careful angular definition of the incident beam, since it is not the goal of this project phase. However, we showed that by restricting the field of view of the bolometer to the signal from the interferometer, the unmodulated offset in the raw spectra can be reduced significantly. We accomplished this by placing a liquid nitrogen soaked piece of
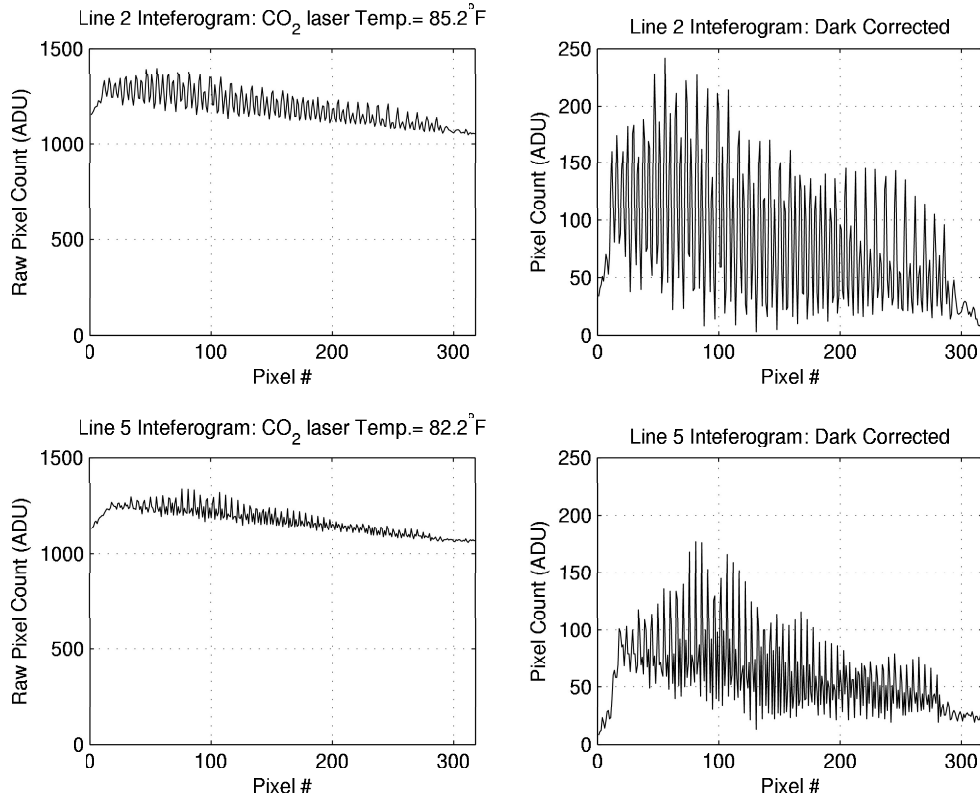
19

Figure 9: *The two left panels show raw interferograms for two CO_2 laser lines (top: $\lambda = 10.653\,\mu m$, bottom: $\lambda = 10.303\,\mu m$). Each interferogram represents a vertical row (slice) of the 2D microbolometer array. The laser tuning was achieved by changing the cavity temperature. The two right panels show the same interferograms after subtracting the background signal that does not originate from the laser (laser on minus laser off). Most of the subtracted nonmodulated signal is due to the fact that the detector field of view is not matched to the interferometer output beam for this breadboard set-up.*

eccosorb® between the detector and the Offner relay, covering parts of the detector FOV that did not view the interferometer beam. This result showed that matching the detector FOV to the interferometer with e.g. a Lyot stop will significantly reduce the nonmodulated offset in the interferogram. We will pursue this strategy in the next phase of this program.

The observation of these high contrast, high spatial frequency fringes was the first major milestone of the breadboard effort. In the following, we will present further data characterizing the breadboard interferometer.

Line	Laser T [°F]	# Fringes per detector width	CO_2 Laser σ [cm^{-1}]
1	86.0	132	973.3
2	85.2	76	938.7
3	84.5	96	951.2
4	83.9	91	947.8
5	82.2	127	970.6
6	81.6	93	949.5
7	80.7	79	940.6

Table 2: *Temperature scanning the CO_2 laser from 86°F to 80.7°F, produced seven discrete spectral lines (see also Figure 10.)*

3.2   Wavelength Calibration and Resolution

One major objective of this work was to show that a solid interferometer, designed and built without any option to make position or angle adjustments, is in fact suitable for LWIR SHS interferometers. As a first step we detemined the difference between the actual Littrow wavenumber and its design value. We desired that difference to be small compared to the bandpass (several μm) of future passive standoff LWIR SHS instruments. This way, the Littrow wavenumber can be placed reliably at the cut-on or cut-off of the bandpass filter.

The Littrow wavenumber and the effective grating angle can be verified using the wavelength calibration of the interferometer. The wavelength calibration of the SHIMCAD breadboard was accomplished by the observation of seven different CO_2 laser lines with known wavelengths. Figure 10 and Table 2 show the observed spatial fringe frequencies and the line positions. Using equation 5, we fit a linear relationship to the data as shown in the top panel of Figure 10. The residuals between the fitted line positions and the CO_2 line positions are illustrated in the lower panel.

The line fitted to the data in Figure 10 implies a Littrow wavenumber of $\sigma_L = 891.5\,\text{cm}^{-1}$ ($\lambda_L = 11.217\,\mu\text{m}$) for which the fringe frequency is zero. Consequently, the actual value of the Littrow wavelength is only $0.033\,\mu$m different from the design value. This difference is indeed small compared to the bandpass and therefore we have shown that the angular grating positioning is suitable for our purposes.
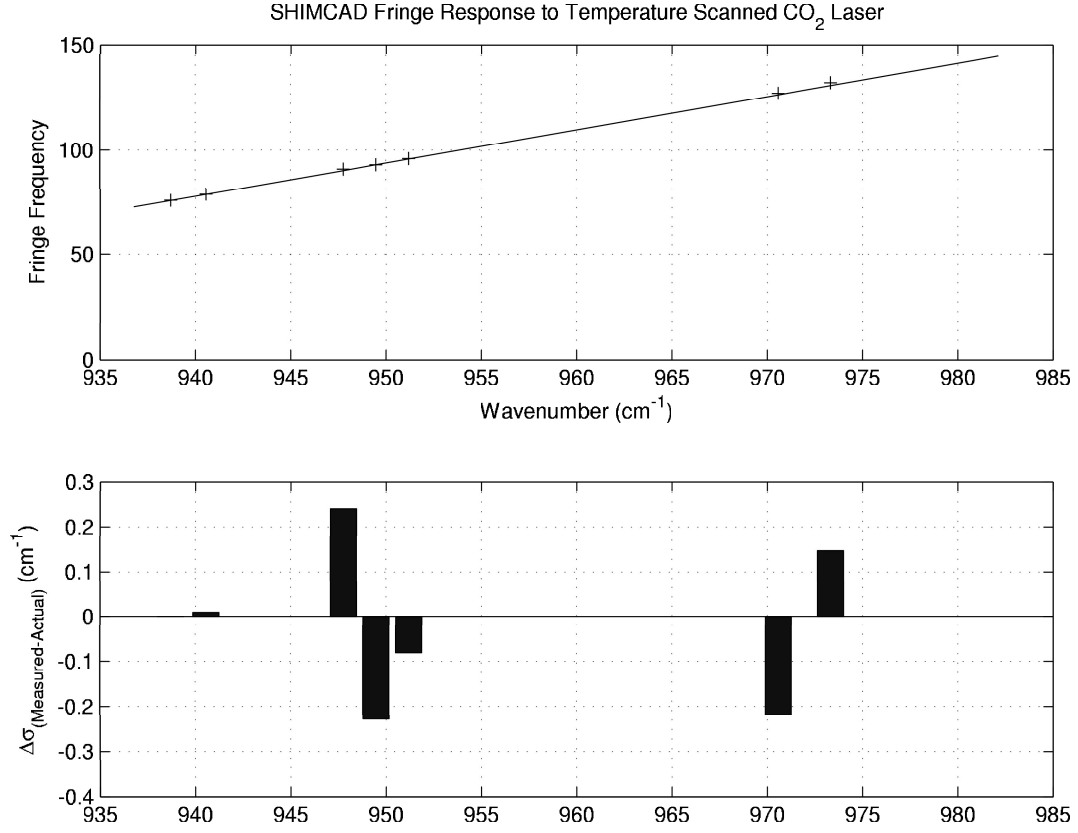
21

Figure 10: *Top panel: Measured fringe frequencies (fringes per detector width) versus* CO_2 *laser line positions. The laser was temperature scanned to select different discrete wavelengths. Bottom panel: Difference between fitted line positions and* CO_2 *line positions. The difference between the actual and fitted wavelengths is less than* $\approx 0.25\,cm^{-1}$

Using the grating groove density (1/d) and the Littrow wavenumber we can calculate the actual effective grating angle:

$$\theta = \arcsin\left(\frac{1}{2\sigma_L d}\right) = 13.59° \tag{7}$$

which is only 0.04° ($\approx$140 arcsec) different from the design value (13.63°). With this grating angle and the actual imaged grating width[3] of 16.7 mm, we can calculate the achieved resolving power at 950 cm^{-1}:

$$R = 4W\sigma\sin\theta = 1491 \tag{8}$$

Another way of calculating the resolving power is to ratio the incident wavenumber with the wavenumber difference that results in one additional fringe in the interferogram. Using the slope of the line in Figure 10 of 0.618 cm^{-1}/fringe around 950 cm^{-1} we get R=950/0.621=1530. This result is within 3% of the result in equation 8, which is a sufficiently accurate verification for this breadboard effort.

3.3 Zero Path Location

Another important check to verify whether the optical components in the interferometer are positioned correctly is to find the ZPD location where the distances of both gratings to the beamsplitter are equal. For this interferometer, the zero path location was designed to be in the center of the gratings. Using a broadband source, like a thermal emitter, the zero path location can be readily identified, because the interferogram has low contrast for essentially all path differences except at zero path difference, where the phases of all fringes line up (location of stationary phase). As with other SHS interferometers that we have built, we expect a so called "barber pole" at the location of zero phase. It gets its name from its tilted stripes, which are the result of a slight grating tilt that causes a small optical path difference between the top and the bottom of the grating, which in turn results in a fringe pattern. Since this fringe pattern is not heterodyned like the one in the dispersion plane, it is roughly the same for all frequencies in the bandpass and therefore does not average out, even for a broadband source. For a perfectly aligned SHS interferometer, the

---

[3]see Section 3.3

gratings are not tilted at all and the barber pole has no stripes. However, this is often not the case and one can observe a few stripes or fringes in the barber pole. In many cases, this grating tilt has no negative effect on the data quality.

The top panel of Figure 11 shows an interferogram taken with the broadband, wire filament source. The image has been enhanced to emphasize the barber pole and to eliminate isolated flatfielding effects. The ZPD location is clearly visible with about seven fringes perpendicular to the dispersion plane.

Seven fringes in the barber pole would be acceptable for a field instrument as planned for the SHIMCAD project (at least 32 vertical FOV slices, see also Figure 2). The barber pole fringes correspond to an effective grating tilt of about 450 arcsec or a displacement between the top and bottom of one grating of about 35 μm.

In order to determine how close the ZPD position is to the center of the gratings we imaged an edge, which was positioned (by hand) at the grating center position (one grating was removed for this measurement and replaced by the edge). At one side of the edge a coil filament was placed as shown in the lower panel of Figure 11. It is obvious from the image of the edge that the grating center is not imaged onto the center of the detector array. This is not surprising because the detector was aligned to yield the best fringe images and the illumination of the gratings was not controlled tightly enough to ensure central illumination of the oversized gratings. However, the comparison of both pannels in Figure 11 shows that the ZPD position is very close to the center of the gratings. The offset between the edge and the barber pole is about 1 mm which is most likely due to the uncertainty of the edge placement, which was done by hand without an adequate mechanical fiducial warranting higher precision.

The horizontal ZPD position for this instrument is quite insensitive to small grating translations along the optical axis. A relatively large translation of about 0.5 mm would be necessary to move the ZDP location by about 1 mm.

The lower panel of Figure 11 was also used to verify the magnification of the exit optics. The intrinsic 1:1 magnification of the Offner could be verified successfully by comparing the object and image size of the coil filament source. An important implication of the 1:1 magnification is that the grating width imaged onto the detector is equal to the detector width, which is about 16.7 mm.
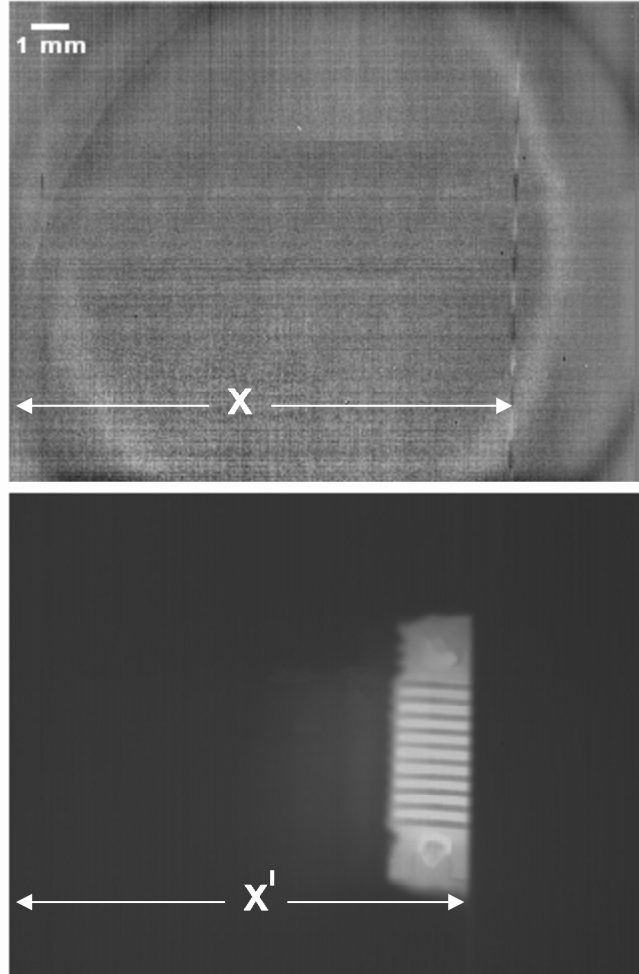
Figure 11: *The upper panel shows the zero path location (location of stationary phase) of the SHIMCAD breadboard interferometer at the distance x from the left side of the detector array edge. The image was enhanced to emphasize the contrast at the ZPD location and corrected for isolated flatfield features away from ZPD. The lower panel shows an edge, x' from the image edge, which was positioned by hand close to the center of the grating, and a filament source on one side of the edge. This image verifies that the ZPD location is close to the grating center, as designed. The difference of 1 mm between x and x' is most likely due to the uncertainty on positioning the edge, which was done by hand.*

3.4 Phase Distortion

Finally, we investigate the phase distortion of the observed fringes. The motivation for this analysis was mainly the phase distortion that is evident in the data from the LANL LWIR SHS [Laubscher et al., 1999] as shown in Figure 12A. In addition to the apparent fringe curvature of this laser line interferogram, one can see a frequency change of the fringe pattern across the detector. Even though moderate phase distortions can be corrected in post processing as demonstrated by Harlander et al. [1994] and Englert et al. [2004], major phase distortions are likely to decrease the data quality in a significant way. In Figure 12 we compare the LANL result with a typical SHIMCAD breadboard fringe pattern. The fringe pattern in Figure 12B is representative of the SHIMCAD interferograms that we measured. To quantify the SHIMCAD breadboard phase distortion we applied the technique of Harlander et al. [1994] to an interferogram equivalent to one row of the 2D data. The result is given in Figure 13. It shows a phase distorion of less than 1.5 fringes for a fringe pattern with 76 fringes across the detector. A small phase distortion like this is readily corrected in post processing as demonstrated by Harlander et al. [1994] and Englert et al. [2004].
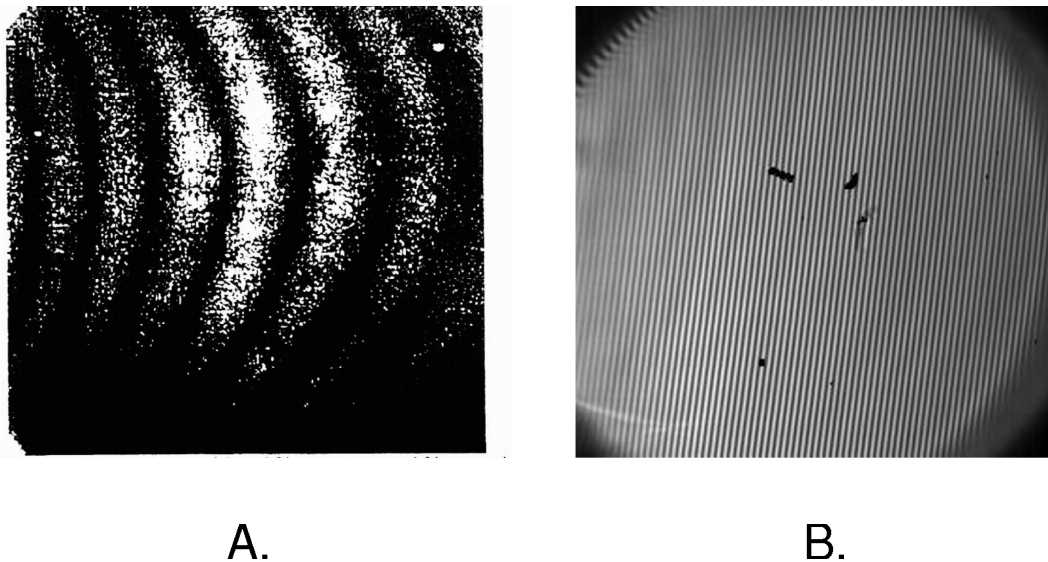
A.   B.

Figure 12: *LWIR fringes recorded at LANL in panel A [Laubscher et al., 1999] compared to a typical fringe pattern recorded at NRL with the SHIMCAD breadboard interferometer in panel B. The NRL data was cropped to 256 horizontal pixels to match the LANL detector. The defects in panel B are due to bad pixels in the detector array.*
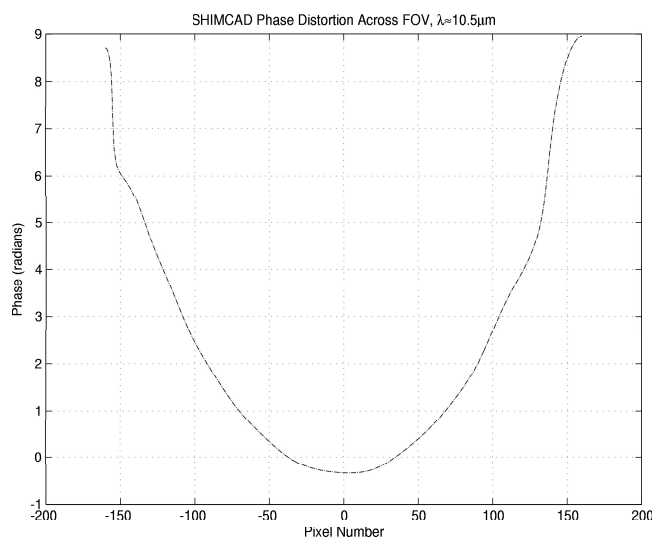

Figure 13: *Phase distortion across the FOV.*

4 Summary

The overall goal of the NRL Spatial Heterodyne IMager for Chemicals and Atmospheric Detection (SHIMCAD) project is to develop an intrinsically rugged, new type of long wave infrared (LWIR) hyperspectral sensor for the passive measurement of atmospheric trace constituents. The project consists of three phases. A breadboard phase, a brassboard phase and a testing phase. This report covers the results of the first phase of the SHIMCAD project which had two major objectives:

- Design and build a non field-widened LWIR SHS breadboard interferometer (1) with primarily off-the-shelf parts and (2) using fixed angles and distances within the interferometer so that no post integration alignment is required.

- Characterize the interferometer's wavelength calibration, phase distortion, and zero path location in order to verify that the approach of fixed optics locations and no alignment possibilities is adequate.

An interferometer was designed and built with a COTS beamsplitter, compensation plate, and gratings. The components were positioned with respect to each other using a solid, two part, aluminum structure without any option of position or angle adjustments. The interferometer was characterized using a broadband source and a tunable CO_2 laser.

Using monochromatic interferograms we performed a wavelength calibration showing that the difference between the achieved Littrow wavenumber and its design value is small ($0.033\,\mu$m) compared to the bandpass. Consequently, the Littrow frequency can be placed reliably at the cut-on or cut-off of the bandpass filter without any post integration alignment. The measured resolving power (R $\approx$ 1500) was found to be consistent with the grating groove density and the illuminated grating width.

Using a broadband source we determined the relative location of the gratings with respect to the beamsplitter and the effective grating tilt (tilt axis in the grating plane and perpendicular to the grating grooves). The relative grating location with respect to the beamsplitter was determined by locating the barber pole at zero path difference, where the gratings are equidistant to the beamsplitter. Within the measurement uncertainty, the zero path location was in the middle of the grating,

as designed. The determination of the grating tilt resulted in a small, acceptable value of ≈ 450 arcsec, or about seven fringes in the barber pole.

The phase distortion has been measured to be less than 1.5 fringes across the detector array for a fringe frequency of 76 fringes per detector width. Small phase distortions, like the ones observed here, are readily corrected in post processing [Harlander et al., 1994; Englert et al., 2004]. No significant fringe curvature was observed.

The results of this successful breadboard effort show that the approach of fabricating a aluminum structure with conventinal CNC tolerances and without alignment options to position the SHS interferometer components is suitable for the SHIMCAD project goals. In this work we were able to measure the first straight monochromatic SHS fringes in the LWIR with a negligible amount of phase distortion. In addition, we showed the first zero path measurement of an LWIR SHS interferometer.

Acknowledgements

References

[Brault, 1985] Brault J.W.: *Fourier Transform Spectroscopy*
High resolution in astromomy: Fifteenth Advanced Course of the Swiss Society of Astronomy and Astrophysics, A. Benz, M. Huber & M. Mayor (Eds.), Sauverny, Switzerland, 1-61, (1985)

[Cardon et al., 2003] Cardon J.G., C.R. Englert, J.M. Harlander, F.L. Roesler, and M.H. Stevens: *SHIMMER on STS-112: Development and Proof-of-Concept Flight*
AIAA Space 2003 - Conference & Exposition, Long Beach, CA, Sept. 23-25 (2003)

[Englert et al., 2004] Englert, C.R., J.M. Harlander, J.G. Cardon, F.L. Roesler: *Correction of Phase Distortion in Spatial Heterodyne Spectroscopy*
Applied Optics **43**, 6680-6687 (2004)

[Englert et al., 2005] Englert, C.R., J.T. Bays, J,C. Owrutsky, J.M. Harlander: *SHIM-Fire Breadboard: Instrument Design, Integration, and First Measurements*
NRL Memorandum Report, NRL/MR/7640–05-8926 (2005)

[Englert and Harlander, 2006] Englert, C.R., J.M. Harlander: *Flatfielding in spatial heterodyne spectroscopy*
Applied Optics **45**, 4583-4590 (2006)

[Hackwell et al., 1996] Hackwell J.A., D.W. Warren, R.P. Bongiovi, S.J. Hasel, T.L. Hayhurst, D.J. Mabry, M.G. Sivjee, and J.W. Skinner: *LWIR/MWIR Imaging Hyperspectral Sensor for Airborne and Ground-Based Remote Sensing*
Proc. SPIE **2819**, 102-107 (1996)

[Hammond and Popa, 2005] Hammond, B. and M. Popa: *Overview of the Joint Services Lightweight Standoff Chemical Agent Detector (JSLSCAD)*
Proc. SPIE **5795**, 86-95 (2005)

[Harlander, 1991] Harlander J.M.: *Spatial Heterodyne Spectroscopy: Interferometric Performance at any wavelength without scanning*
Ph.D. dissertation (Univ. of Wisconsin-Madison), Madison WI (1991)

[Harlander et al., 1992] Harlander J.M., R.J. Reynolds, and F.L. Roesler: *Spatial heterodyne spectroscopy for the exploration of diffuse interstellar emission lines at far ultraviolet wavelengths*
Astrophysical Journal **396**, 730-740 (1992)

[Harlander et al., 1994] Harlander J.M., H.T. Tran, F.L. Roesler, K.P. Jaehnig, S.M. Seo, W.T. Sanders, and R.J. Reynolds: *Field-Widened Spatial Heterodyne Spectroscopy: Correcting for Optical Defects and New Vacuum Ultraviolet Performance Tests*
Proc. SPIE **2280**, 310-319 (1994)

[Harlander et al., 2002] Harlander J.M., F.L. Roesler, J.G. Cardon, C.R. Englert, and R.R. Conway: *SHIMMER: A Spatial Heterodyne Spectrometer for Remote Sensing of Earth's Middle Atmosphere*
Applied Optics **41**, 1343-1352 (2002)

[Harlander et al., 2003] Harlander J.M., F.L. Roesler, C.R. Englert, J.G. Cardon, R.R. Conway, C.M. Brown, J. Wimperis: *Robust monolithic ultraviolet interferometer for the SHIMMER instrument on STPSat-1*
Applied Optics **42**, 2829-2834 (2003)

[Laubscher et al., 1999] Laubscher B.E., B.W. Smith, B.J. Cooke et al.: *The Infrared Imaging Spatial Heterodyne Spectrometer (IRISHS) experiment effort*
Proc. SPIE **3701**, 194-205 (1999)

[Lucey et al., 1998] Lucey P.G., T. Williams, M. Mignard, J. Julian, D. Kokobun, G. Allen, D. Hampton, W. Schaff, M. Schlangen, E.M. Winter, W. Kendall, A. Stocker, K. Horton, A.P. Bowman: *AHI: An airborne long wave infrared hyperspectral imager*
Proc. SPIE **3431**, 36-43 (1998)

31

[Marinelli et al., 1998] Marinelli J.W., C.M. Gittins, A.H. Gelb, B.D. Green: *Tunable Fabry-Perot etalon-based long wave infrared imaging spectroradiometer*
Applied Optics **38**, 2594-2604 (1999)

[Pritt et al., 1998] Pritt A.T., P.N. Kupferman, S.J. Young, R.A. Keller: *Imaging LWIR Spectrometers for Remote Sensing Applications*
Proc. SPIE **3063**, 138-149 (1997)

[Schildkraut et al., 2002] Schildkraut E.R., R.F. Connors, A. Ben-David, A. Ifarraguerri: *An ultra-high sensitivity, passive FTIR sensor (HiSPEC) and initial field results*
Proc. SPIE, **4574**, 18-25 (2002)

[Schildkraut et al., 2004] Schildkraut E.R., T.G. Quinn III, C. Fehser, R. Connors, R. Mitrano, and J.O. Jensen: *Ultra-sensitive, versatile FTIR spectrometer for sub-lethal chemical identification and biological agent cueing (HiSPEC-II)*
Sixth Joint Conference on Standoff Detection for Chemical and Biological Defence, Williamsburg, VA, Oct. 25-29 (2004)

[Sellar and Boreman, 2005] Sellar R., and G.D. Boreman: *Comparison of relative signal-to-noise ratios of different classes of imaging spectrometer*
Applied Optics **44**, 1614-1624 (2005)

[Smith and Harlander, 1999] Smith B.W. and J.M. Harlander: *Imaging spatial heterodyne spectroscopy: theory and practice*
Proc. SPIE, **3698**, 925-931 (1999)

[Vallières et al., 2005] Vallières A., M. Chamberland, V. Flarley, L. Belhumeur, A. Villemaire, J. Giroux, J.-F. Legault: *High Performance Field Portable Imaging Radiometric Spectrometer Technology for Chemical Agent Detection*
Proc. SPIE, **5990**, 59900U (2005)

[Wadsworth and Dybwad, 2002] Wadsworth W. and J.P. Dybwad: *Rugged high speed rotary imaging Fourier Transform Spectrometer for industrial use*
Proc. SPIE **4577**, 83-88 (2002)